Journal of Fluids and Structures (1998) **12,** 103–121

THE INFLUENCE OF STRUCTURAL DEFORMATION ON WATER JET IMPACT LOADING

G. L. CHAHINE AND K. M. KALUMUCK
DYNAFLOW Inc., 7210 Pindell School Road
Fulton, MD 20759, U.S.A.

(Received 25 March 1997 and in revised form 10 September 1997)

The collapse of an underwater explosion bubble near a solid structure is accompanied by the formation of a high-speed re-entrant liquid jet. The intensity of this jet and the pressure loading generated on the body are functions of the characteristics of both the explosion bubble and the structure. The dynamics of the structure and the bubble are *fully* coupled. Boundary motions can modify the bubble dynamics and re-entering jet characteristics. The structure response also modifies the jet loading due to jet impact. To study the modification of the jet impact loading due to the structural response, a series of simple, well-controlled experiments were conducted. Water jets of known characteristics were impacted on plates of varying flexibility and their response and the pressure loads measured. Substantial reduction in peak load is seen due to the presence of plate flexibility. Similar results were obtained using our bubble dynamics code, 2DYNAFS, coupled to a structural dynamics code, NIKE2D, to study the coupled response of a deformable interacting structure and a nearby bubble. Results of both the experimental and numerical studies highlight the need for utilizing *fully coupled* calculations of explosion bubble loading on structures.

1. INTRODUCTION

THE INTERACTION of an underwater explosion with a nearby submerged structure is a complex phenomenon involving several successive stages. Following detonation, a shock wave is generated which initially loads the structure. The detonation also produces a bubble, composed of the gaseous explosion products, which rapidly grows beyond its equilibrium size and then collapses nonspherically. In the presence of a nearby solid structure, this bubble collapse may be accompanied by the formation of a high-speed re-entrant liquid jet directed towards the structure. When the explosive is detonated sufficiently close to the structure, the high-speed re-entrant jet may impact the body, resulting in a very large loading.

The amplitude of the pressures generated on the structure during the explosion phenomenon is a function not only of the characteristics of the explosion bubble, but also of the structure. This is consistent with impact phenomena in general, where the impact phenomena depend on the characteristics of both bodies or substances being impacted together.

Due to the complexity of a fully coupled calculation, structural response computations have typically been conducted using loads obtained from fluid code computations of bubble dynamics near undeformable boundaries of the same geometry [e.g. Kiddy & McDonald (1994)]. Loads obtained from these rigid-boundary calculations were then mapped onto the structural model which was used to calculate the structural response to the applied loads.

0889–9746/98/010103 + 19 $25.00/fl970127

More recently, fully coupled computations have begun to be developed (Chahine *et al.* 1997).

In reality, the dynamics of the structure and the bubble dynamics are *fully* coupled. Boundary motions (e.g. translation and/or deformation) can modify the bubble dynamics and re-entering jet characteristics such as jet velocity and mass. Even for cases where the structural motions do not affect the bubble dynamics and jet formation, it is expected that the local structural response will modify the jet loading. Reductions in the loading (compared to the rigid case) will be caused by motions of the structure as it reacts to the load, and by absorption of energy in the structure as it deforms.

In order to study the influence of the structural motion on the loads generated by an impacting liquid jet, a series of experiments utilizing well-characterized water jets of known speed and size were conducted. The jets were impacted on metal plates, and the pressures generated at the plate surface as well as the plate displacements were measured as functions of time. The objective of this work was to conduct simple controlled experiments to quantify the modification of water-jet impact loading due to fluid–structure interactions. The results could then provide fundamental experimental data for code development and validation.

Recently, Boùrne *et al.* (1997) investigated damage mechanisms in brittle materials from higher speed (600 m/s) jet impact using high-speed photography but did not consider loading differences due to structural response. Lesser (1981) provides analytical solutions to the early stages of drop impact on rigid and elastic surfaces. Bourne *et al.* (1996) and Oguz *et al.* (1995) investigate experimentally and numerically the problem of liquid-column impact onto a liquid-free surface. The dynamics of this problem differ significantly from that of impact on a solid surface.

In a parallel effort, the effects of structural flexibility were assessed using our Boundary Element Method code, 2DynaFS, coupled to a Lawrence Livermore National Laboratories Finite Element Method structural dynamics code, NIKE2D. The resulting coupled code was used to model the response of a deformable structure interacting with a nearby bubble.

2. EXPERIMENTAL SET-UP

Experiments were conducted in the Dynaflow Water Jet Laboratory. The experimental set-up consisted of a diesel pump, a translating carriage and a rigid stand that held the test plates and the supporting instrumentation. Front and side views of the test-stand set-up are provided in Figure 1. The pump was a Weatherford five-plunger positive displacement pump, driven by a 112 kW (150 hp) diesel engine, and capable of delivering a flow rate of approximately 1·4 l/s at pressures up to 69 MPa.

Figure 2 provides a close-up view of the nozzle and plate. The nozzle assembly was affixed to a translating carriage. As this carriage moved horizontally below the horizontal target plate, the target plate was shielded from the jet by a splash guard affixed to the test stand (Figure 1). In the centre of the splash guard, a hollow tube ("slug alignment tube") enabled part of the jet to pass through, creating a slug of water which then impacted on the target plate. In this procedure, the velocity of the jet exiting the nozzle is steady and known. Use of the translating nozzle also enabled control of slug length, which is determined by the combination of the jet velocity and the carriage translation velocity. This allowed a high degree of control over the jet characteristics. In contrast, acceleration of a water slug is more difficult, having the added uncertainties of the velocity to which the slug is accelerated and whether this velocity is uniform throughout the impact event.

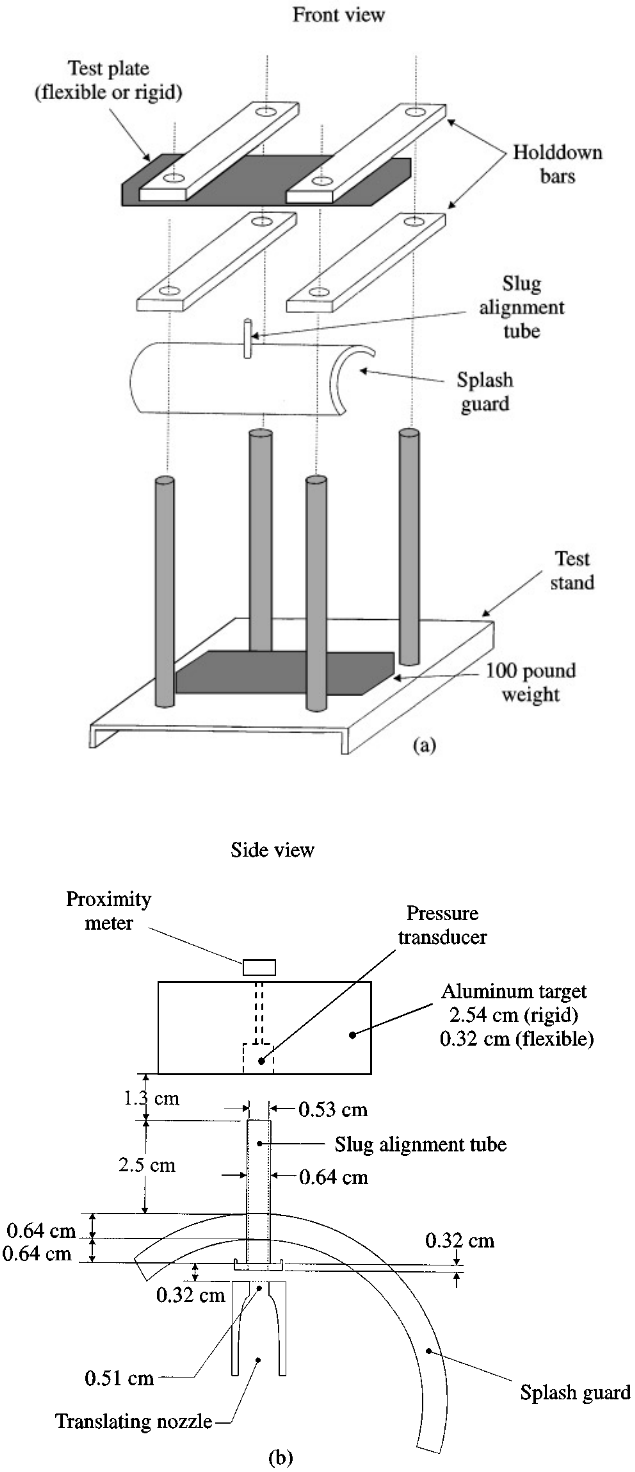

Figure 1. Front and side views of experimental set-up.

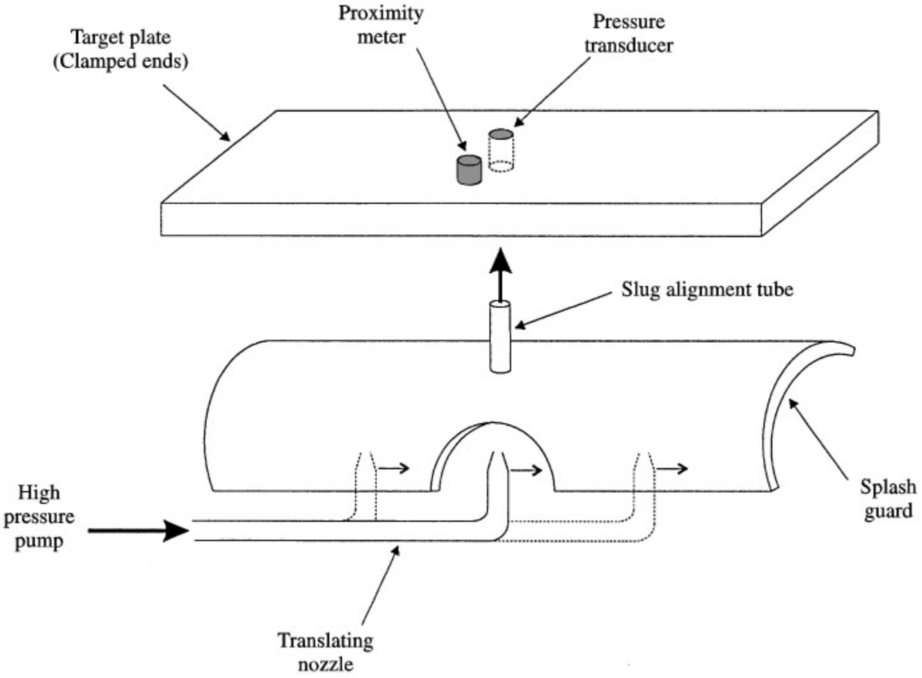

Figure 2. Sketch of water slug generation system. Flow rate and nozzle translation velocity determine slug length and velocity.

The target plates were held in place by clamping between two pairs of 5 cm wide aluminium bars. The assembly was held together with all-thread rods affixed to the test-stand base which was anchored with a 45 kg weight. Two test plates were used during this experiment: (a) a 2·54 cm thick aluminium "rigid" plate; and (b) a 0·32 cm thick aluminium "flexible" plate.

The terms "flexible" and "rigid" refer to the amplitudes of the characteristic deflections of the plates. The plates were held in a fashion which eliminated any potential translation or rotation during impact, allowing only pure bending motion.

A pressure transducer was mounted in the test plate centred above the slug alignment tube and thus directly exposed to the impacting slug. The transducer was a PCB Piezotronics ICP quartz pressure transducer, with a sensitivity of 72 mV/MPa (0·5 mV/psi), an active area diameter of 0·53 cm and a 500 kHz resonance frequency. A Metrix eddy current proximity sensor was mounted above the test plate (i.e. on the back of the plate) to measure plate deflections during the test. This proximity sensor had a sensitivity of 8 mV/μm (200 mV/mil) and a flat frequency response from 0 to 10 kHz. Data were collected with a Gould four-channel digital storage oscilloscope and transferred to a PC via GPIB connection for analysis.

3. EXPERIMENTAL RESULTS

3.1. Observations

Both plates were tested at nozzle pressure drops corresponding to jet velocities between 37 and 98 m/s, which covers a range of interest to underwater explosions, and over a range of horizontal carriage translation velocities between 0·11 and 0·57 m/s.

The carriage translation velocity, V_t, determines the length, L, of the water slug which is given by

$$L = \frac{V_j d_0}{V_t}, \tag{1}$$

where d_0 is the slug alignment tube diameter (0·53 cm) and V_j is the jet velocity. The value of L thus ranged from 0·86 to 4·6 m. The duration of the slug, T_s, is inversely related to the jet translation velocity:

$$T_s = \frac{d_0}{V_t}. \tag{2}$$

The value of T_s varied from 0·009 to 0·047 s.

Figure 3 presents photographs of the water slugs generated as they exit the slug alignment tube. Figure 3(a) shows the slug exiting the alignment tube in the absence of a plate. Figures 3(b, c) presents photographs of the slug in the presence of the 2·54 cm plate just prior to and following impact. It can be seen that the slug spreads out radially along the surface following impact and that the slug remains a coherent column of liquid prior to and during impact. Small nonuniformities of the leading edge of the slug were caused by surface instabilities, which led to the formation of some droplets.

3.2. MEASURED PRESSURES AND DEFLECTIONS

Figure 4 presents a sample of the raw data obtained from the pressure transducer and proximity meter for the case of the 0·32 cm thick flexible plate with a jet exit velocity of 91 m/s and a slug length of 0·86 m. As can be seen in this figure, the signals contain only a low amplitude of high-frequency noise, and the overall response is readily discerned. (The high-frequency noise is believed to be due to some oscillation frequency of the set-up and not a ringing of the pressure transducer. This set-up oscillation frequency is of the order of 700 Hz, while the transducer resonant frequency is 500 kHz.) The peak values of the measured pressure and displacement occur approximately simultaneously 0·015 s following the beginning of the pressure rise. The rise in the measured pressure is initially more rapid than that of the plate displacement due to the inertia of the plate. Both signatures are fairly broad: the pressure signal is positive for about 0·025–0·030 s while the displacement peak width is about 0·02 s. Both signals decline monotonically from their peak and pass through zero nearly simultaneously as the plate, having been excited by the jet impact, oscillates in the opposite direction.

The high-frequency noise can be removed by utilizing a simple moving average in time. The results of such a smoothing are presented in Figure 5 for the raw data of Figure 4 and exhibit a very smooth behaviour. Typically, a set of ten runs were performed and ensemble averaged. Details of data repeatability, which was fairly good, can be found in Chahine *et al.* (1995).

Systematic experiments at each jet velocity were performed at fixed slug durations (carriage translation speeds). Figure 6 presents the measured maximum (peak) impact pressures for the case where the slug duration was $T_g = 0{\cdot}023$ s for both the rigid and flexible plates. Each data point on this plot represents an average of the maximum impact pressure over a series of 10 runs under the same conditions. The peak-measured impact pressures are plotted against the jet stagnation pressure, P_{stag},

$$P_{\text{stag}} = \tfrac{1}{2}\rho V_j^2, \tag{3}$$

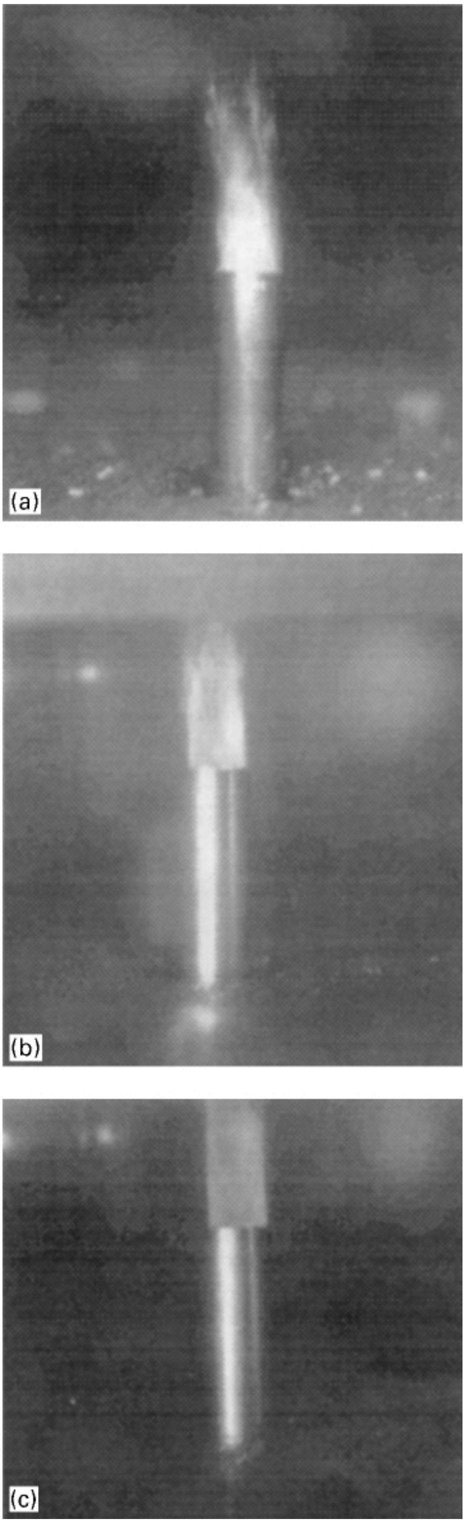

Figure 3. Photographs of water slug development and impact: (a) exiting alignment tube; (b) prior to impact; (c) following impact.

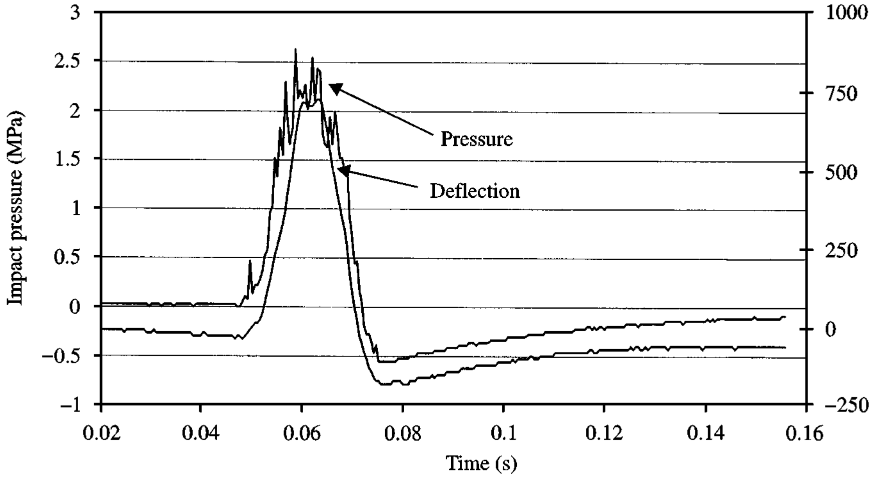

Figure 4. Sample pressure transducer and proximity meter raw data for the flexible plate case. Jet: 91 m/s—L_{slug}; 0·86 m.

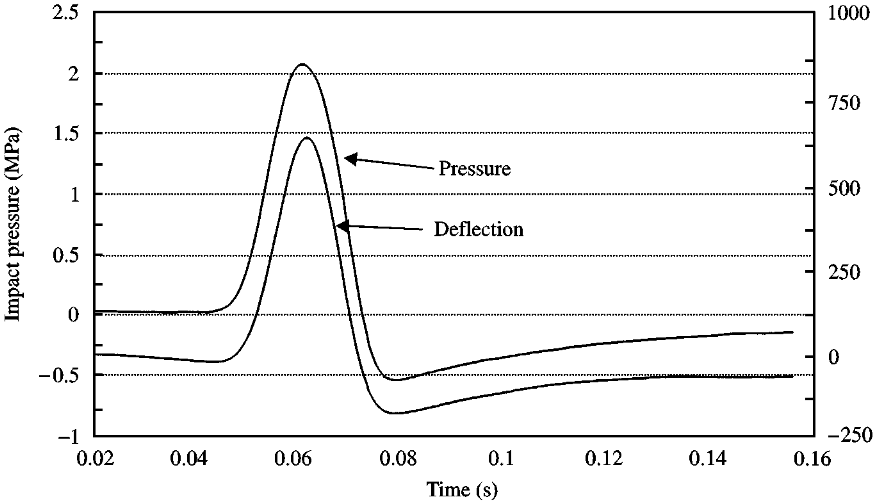

Figure 5. Results of smoothing of raw data presented in Figure 4 with a moving average. Jet: 91 m/s—L_{slug}; 0·86 m.

where ρ is the liquid density. (Note that V_j is the nozzle exit jet velocity and not the impact velocity). As can be seen from this plot, the measured impact pressure varies approximately linearly with calculated jet stagnation pressure. However, the value of the impact pressure is seen to be consistently less than the jet stagnation pressure. This is to be expected, since the jet exiting the nozzle has been modified in the alignment tube and during its traverse to the target. Also, the impacted boundary is not perfectly rigid and immovable even for the 2·54 cm thick plate, as can be seen by the proximity meter measurements described below. During impact, stress waves are set up in the plate (and also in the liquid slug), which also dissipate energy.

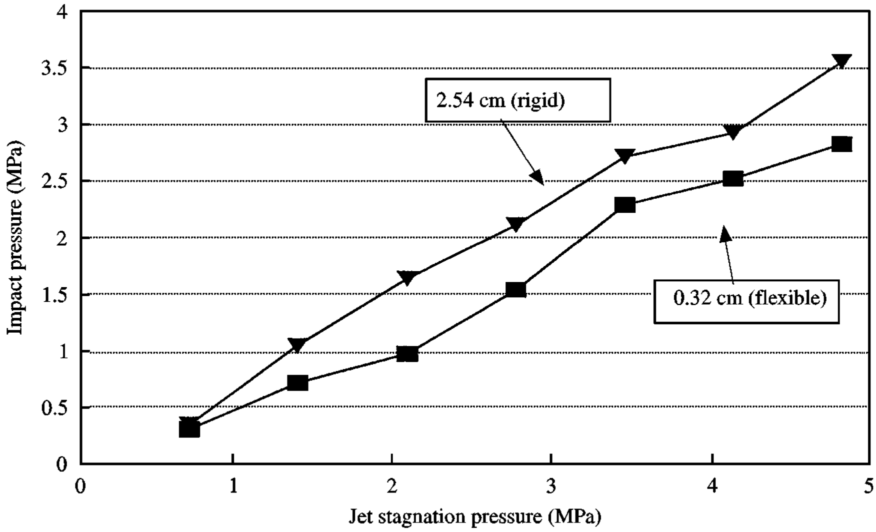

Figure 6. Maximum measured rigid and flexible plate impact pressures as functions of calculated jet stagnation pressure. Slug duration 0·023 s.

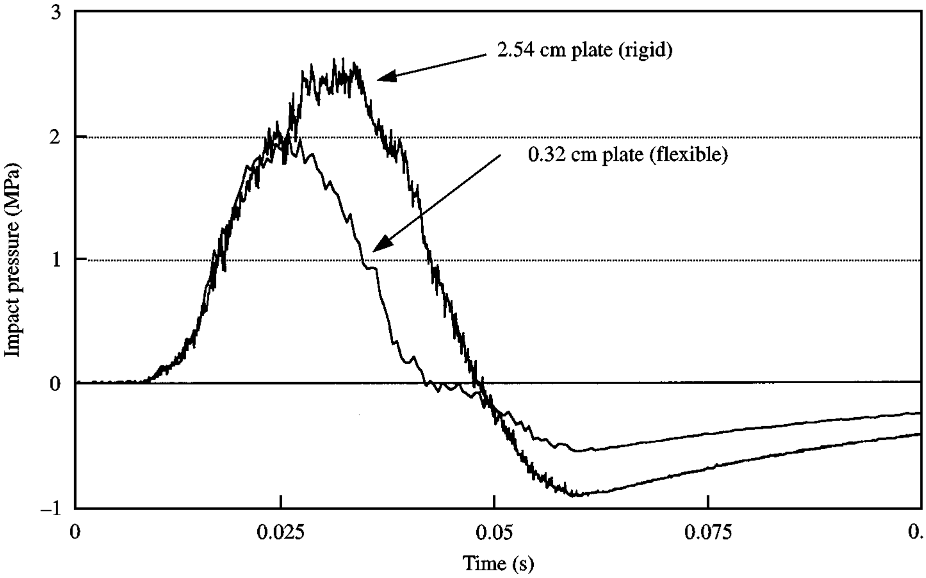

Figure 7. Comparison of measured rigid and flexible plate impact pressure histories. Data averaged over 10 runs. Jet: 91 m/s—L_{slug}; 1·6 m.

Important for our objectives here is the comparison of the impact pressures generated for the rigid and flexible plate cases. Figure 7 compares measured impact pressure histories for the rigid and flexible plates for the case of $V_j = 91$ m/s and a slug length $L = 1{\cdot}6$ m. The flexible plate is seen to both reduce the peak amplitude of the impact pressure and to

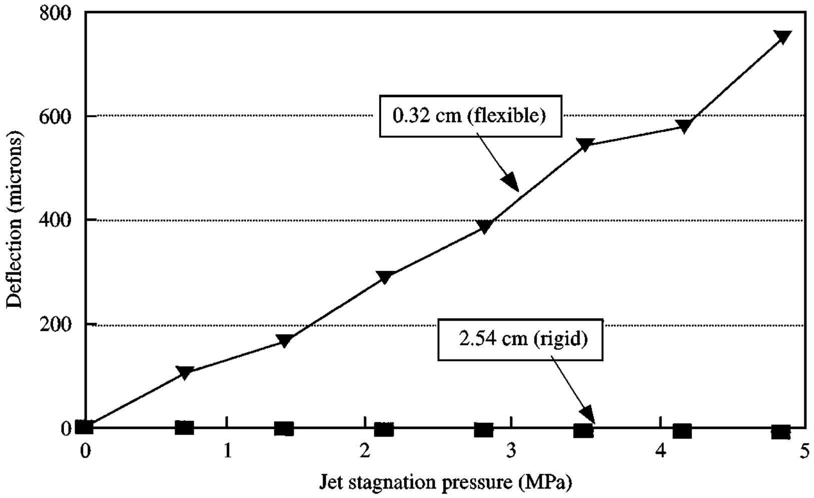

Figure 8. Maximum measured rigid and flexible plate deflections as functions of calcculated jet stagnation pressure. Slug duration 0·023 s.

shorten the duration of the impact pressure pulse from that of the rigid plate. As can be seen in Figure 6, at low jet stagnation pressures, there is little or no difference in the measured impact pressure for the two plate thicknesses. At higher stagnation pressures, however, the measured maximum impact pressures for the flexible plate case are significantly less than those of the rigid-plate case. The measured maximum impact pressure for the flexible plate varied between 55 and 80% of that of the rigid plate for jet stagnation pressures between 1·4 and 4·8 MPa (jet exit velocities between 52 and 98 m/s).

This demonstrates that *following impact of a liquid jet, boundary deformation of the impacted target can substantially affect the load felt by the structure.*

Figure 8 presents the maximum measured deflections for this case. Comparison of Figures 6 and 8 shows that the measured deflections are basically tracking the behaviour of the impact pressure for the flexible plate. The rigid-plate deflections are seen to be negligible.

3.3. IMPACT DURATION

It is instructive to examine the duration of the measured pressure pulses and plate deflections and to relate these to the slug impact event duration. Figure 9 presents a sketch that defines the pulse widths labelled as T1 and T2 for the pressure and deflection pulse widths, respectively. It was found that the width of the signal, of pulse, measured at a level 80% below the maximum value (i.e. at 0·2 times the peak value) was a better measure of the pulse duration than measurement of the full pulse width (denoted as the 100% value) because of small initial slopes of the signals leading to large uncertainties in this width. The 80% pulse width value was found to be an excellent and repeatable measure for both the pressure and deflection data. This can be seen in Figure 10, which presents data sets for a 91 m/s jet impacting the flexible plate over a range of slug durations (slug lengths). One would expect a relation of the form

$$T = C\frac{d_0}{V_t} = C\frac{L}{V_j}. \tag{4}$$

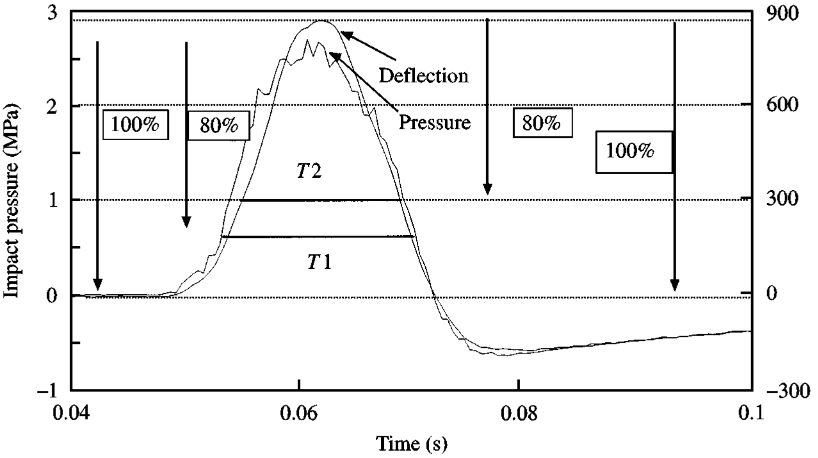

Figure 9. Sketch defining pulse-width measurement for pressure and deflection.

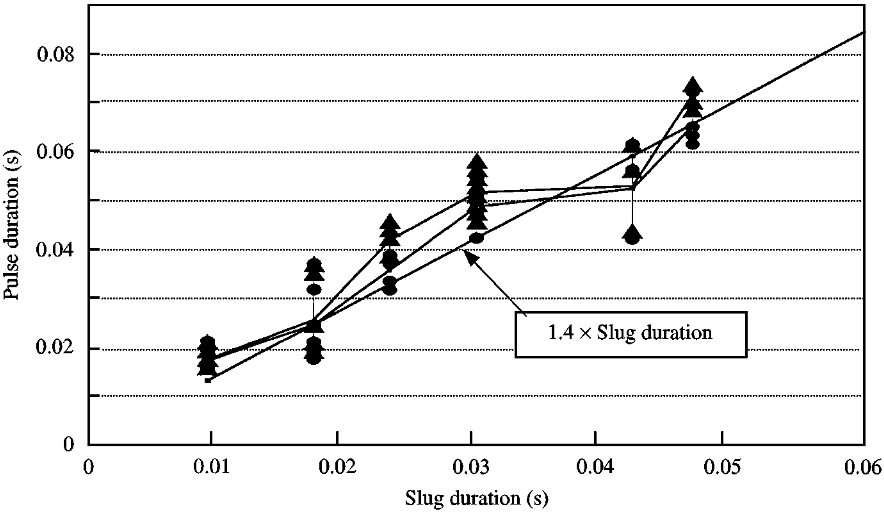

Figure 10. Measured pressure and deflection 80% pulse widths as functions of slug duration for 91 m/s jet on flexible plate: ▲, Proximity meter; ●, transducer.

Here, T is the pulse duration, C is a constant of proportionality, and relations (1) and (2) have been employed. Both the pressure and deflection data are seen to be fit well by a curve of the form (4) with a value of $C = 1{\cdot}4$. The fact that $C > 1$ is a reflection of the use of the 80% pulse-width measure and of the jet velocity modification prior to impact.

3.4. Influence of Slug Characteristics

Results of a range of slug durations (and thus slug lengths) for a single-jet velocity are presented in Figure 11. Slug durations of 0·009–0·047 s (corresponding to slug lengths of

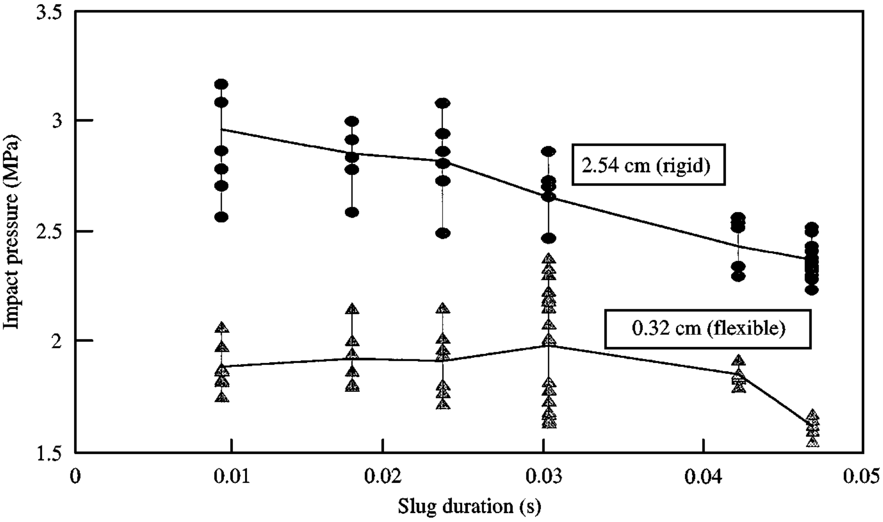

Figure 11. Comparison of maximum measured impact pressures for rigid and flexible plates as functions of slug duration. Jet velocity 91 m/s.

0·86–4·3 m) were used at a jet velocity of 91 m/s. It can be seen from this plot that the maximum impact pressures recorded for both plates initially increase with decreasing slug duration and then converge rather quickly to a value that is essentially independent of the slug duration T_s for $T_s \leq 0{\cdot}023$ s (slug length $L \leq 2{\cdot}1$ m). Again, the flexible plate experiences a smaller load than the rigid plate over the full range of translation velocities investigated. The flexible plate impact pressure is approximately 70% that of the rigid plate in the region of results that are independent of T_s. Basically, an actual unsteady slug impact phenomenon is encountered at the shorter slug durations, while a close to continuous jet stagnation flow is seen for the longer slug durations.

The degree of scatter in the experimental data is also illustrated in this figure. The data form a relatively narrow band about the mean values. The differences between the rigid and flexible plate data are substantially larger than the scatter.

Figure 12 presents maximum plate deflections at a jet velocity of 91 m/s. The results exhibit no particular trend and are relatively independent of slug duration. That the 2·54 cm plate was behaving in a rigid manner can be assessed from these data. Its maximum displacement is seen to be only of the order of a few microns, while that of the flexible plate is seen to be about 250 times greater. This relative magnitude of the displacements is consistent with analytic estimates made by considering a static loading for the two plates. (In reality, the loading is not static. However, this simplification should provide a rough comparison.) The displacement, w, of a given plate of thickness h subject to a load P varies as (Timoshenko & Woinowsky-Krieger 1959)

$$w \sim Ph^{-3}. \qquad (5)$$

This relation predicts that the displacement of the 0·32 cm plate will be 512 times that of the rigid one. However, with a loading of 60% of the rigid plate, the static loading displacement of the 0·32 cm plate would be about 307 times that of the 2·54 cm plate, which is very comparable to the factor of 250 observed in the actual dynamic loading case.

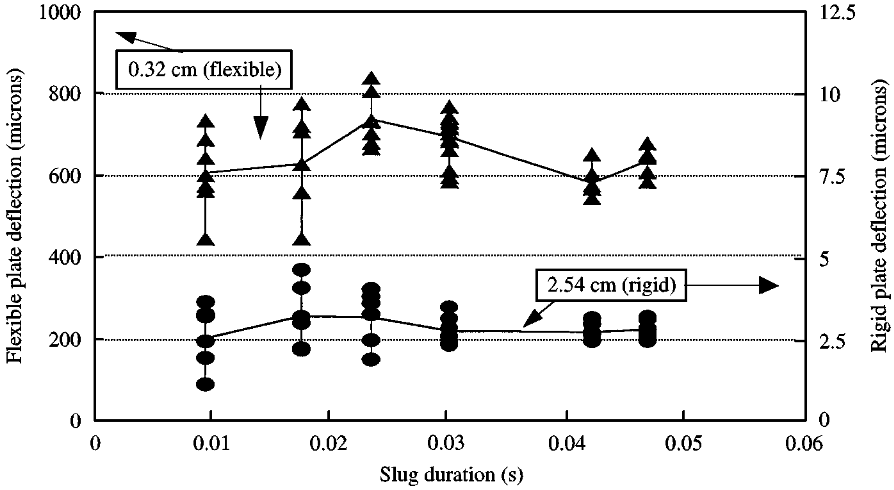

Figure 12. Comparison of maximum measured deflections for rigid and flexible plates as functions of slug duration. Jet velocity 91 m/s.

3.5. STRAIN ENERGY AND DEFORMATION

In order to interpret the results, let us consider the following analysis. In our experiments, the plate was clamped along two edges, while the other two edges were free to move. We shall thus approximate the resulting deformed shape as independent of the transverse direction y. In addition, we shall use as a first fit for the deflection variation with x:

$$w = W \sin\left(\frac{\pi x}{a}\right), \tag{6}$$

where W is the plate displacement at its centre ($x = 0$) and corresponds to the displacement measured in the experiments.

Given a rectangular plate with thickness h, dimensions $a \times b$, and displacement independent of the transverse direction, the strain energy, S_E, stored in the plate due to elastic deflection of the plate is given by (Harris & Crede 1976)

$$S_E = \frac{Eh^3}{24(1-\mu^2)} b \int_0^a \left(\frac{\mathrm{d}^2 w}{\mathrm{d}x^2}\right)^2 \mathrm{d}x, \tag{7}$$

where $w(x, y, t) = w(x, t)$ is the deflection of the plate in the z-direction at any point (x, y) and time t, E is Young's modulus and μ the Poisson ratio. (For aluminium, $E = 6{\cdot}9 \times 10^{10}$ Pa, $\mu = 0{\cdot}33$).

Combining these expressions, one obtains

$$S_E = \frac{Eh^3 \pi^4 b W^2}{48(1-\mu^2)a^3}. \tag{8}$$

Evaluation of this expression yields for the flexible plate

$$S_E = 3{\cdot}05 \times 10^4 \, W^2 \text{ J}, \tag{9}$$

and for the rigid plate

$$S_E = 1{\cdot}75 \times 10^7\, W^2\ \mathrm{J}. \tag{10}$$

One can similarly estimate the work, U, done by an applied force, F, in deflecting the plate an amount w beneath a force, F, by using Castigliano's theorem (Den Hartog 1952):

$$\frac{\partial U}{\partial F} = w. \tag{11}$$

The instantaneous applied force can be written as the product of the spatially averaged impact pressure P_{imp} and the area A impacted by the jet,

$$F = P_{\mathrm{imp}} A. \tag{12}$$

Referring to Figure 4, the rise-to-peak values of both the measured displacement and impact pressure is approximately linear with time. Furthermore, as a first approximation, we consider the response to be linear elastic and take the displacement to be proportional to the load:

$$w = W_{\max} \frac{P_{\mathrm{imp}}}{P_{\max}}, \tag{13}$$

where peak impact conditions $(W_{\max}, P_{\max})$ occur at $t = T$. Substituting equation (13) into equation (11), one can perform the integration:

$$U = \int_0^{F(T)} w \,\mathrm{d}F = \int_0^{T} w(t) \frac{\mathrm{d}F(t)}{\mathrm{d}t}\,\mathrm{d}t \tag{14}$$

$$= \int_0^{P_{\max}} A\left(W_{\max} \frac{P_{\mathrm{imp}}}{P_{\max}}\right) \mathrm{d}P_{\mathrm{imp}} = \frac{W_{\max} P_{\max} A}{2}.$$

Taking the impacted area to be that of the jet cross-section, a circle of diameter 0·53 cm and evaluating expressions (9), (10) and (14) at maximum displacement for the case of 91 m/s jet velocity and a 0·009 s slug duration (0·86 m slug length), and using the data of Figures 11 and 12, we obtain the data in Table 1.

The calculated strain energies are very comparable to the estimated work of deformation calculated using both measured displacements and impact pressures.

The requirement for a decrease in impact pressure due to flexibility can be demonstrated by the following simple argument utilizing the strain energy and work relations above. Equating the ratios of strain energies and work done for the rigid and flexible cases (denoted by superscripts R and F), we have, using equations (9), (10) and (14):

$$\frac{S_E^F}{S_E^R} = 0{\cdot}0017 \left(\frac{W^F}{W^R}\right)^2 = \frac{W^F P_{\max}^F}{W^R P_{\max}^R}. \tag{15}$$

Thus,

$$\frac{P_{\max}^F}{P_{\max}^R} = 0{\cdot}0017 \left(\frac{W^F}{W^R}\right). \tag{16}$$

For the 91 m/s jet case considerd in Table 1, the plate displacement ratio is 240. By relation (16), the flexible plate pressure would be reduced to 41% of the rigid-plate pressure. The experimentally measured values show a reduction of the flexible-plate pressure to 65% of

TABLE 1
Strain energies and work for the rigid and flexible plates

Plate	W_{max} (μm)	P_{max} (MPa)	Strain energy (J)	Work (J)
Rigid	2·5	3·3	0·00011	0·00009
Flexible	610	2·1	0·011	0·014

the rigid-plate value. The difference in these values can be attributed to the approximations made in this simple analysis and to experimental uncertainty. However, the basic concept of a reduction in impact pressure due to target flexibility is demonstrated.

4. SIMULATION RESULTS

This section presents results of example calculations performed utilizing the coupled 2DYNAFS–NIKE2D code. 2DYNAFS is an axisymmetric free-surface Boundary Element Method (BEM)-based code. This code, together with 3DYNAFS™, a fully three-dimensional version of the code, has been developed at DYNAFLOW and used extensively in the modelling of underwater explosion bubble dynamics. [See, for example, Chahine *et al.* (1997) and Chahine & Duraiswami (1993)]. NIKE2D is a powerful finite element method (FEM)-based structural dynamics code developed by Lawrence Livermore National Laboratories (Englemann & Halquist 1991). Coupling of these two codes enables one to take advantage of the strengths and efficiencies inherent in each code: accurate free-surface hydrodynamics and sophisticated structural and material models. Details of this work can be found in Kalumuck *et al.* (1995) and Chahine *et al.* (1997).

A complete coupling of the fluid and the structure is employed at the wetted surfaces of the structure. Calculations are performed at each time step for both the fluid and the structure. The time-step size is determined by the bubble dynamics of the fluid code. Pressures calculated in the fluid are passed to the structure as loads, and the structural dynamics equations solved over the specified time step with these new loads. Velocities and displacements calculated by the structure code are then passed to the fluid code to be employed as new boundary conditions. The normal componet of the gradient of the fluid velocity potential at each node is set equal to the velocity normal to the structure at each node along the wetted surface, and the position of each node is updated based on the calculated displacements. The algorithms are structured such that the fluid code is the "main" routine while the structural code functions as a set of sub-routines driven by the "main" fluid routine.

In the calculations presented here, characteristic length, pressure and time scales are given by R_{max}, the maximum radius the bubble would achieve in an infinite medium; P_0, the ambient pressure at the location of the initial centre of the bubble; and T, the Rayleigh bubble time—the natural period of a bubble in an infinite medium and in the absence of gravity given by

$$T = R_{\max}\sqrt{\frac{\rho}{P_0}}. \tag{17}$$

We first consider a bubble of initial radius $R_0 = 0{\cdot}177$ m, and initial gas pressure $P_{g0} = 6{\cdot}83$ MPa growing and collapsing in a gravity field at a depth of 189 $R_{\max}$ above a spherical structure of radius 4 $R_{\max}$. The sphere is hollow, with a thickness of 0·075 $R_{\max}$, The bubble is taken to be composed of both vapour and noncondensible gas which is assumed to behave polytropically such that $P_g = P_{go}\,(\mathscr{V}_0/\mathscr{V})^k$. Here P_g and $\mathscr{V}$ are the gas pressure and volume, respectively, the subscript o refers to initial conditions, and k is a polytropic constant such that $1 < k < c_p/c_v$, the specific heat ratio. The value used in these calculations is $k = 1{\cdot}25$. This results in a value of $T = 0{\cdot}0146$ s. The material model is *linear elastic* with Young's modulus $E = 8960$ MPa, Poisson ratio $\nu = 0{\cdot}3$, with a a total mass $M = 225$ times the mass of water displaced by the bubble at its maximum size. The interior of the sphere is pressurized to P_o to ensure initial equilibrium.

The bubble was discretized into 30 axisymmetric panels, and the spherical structure was discretized using four-noded axisymmetric continuum elements. In the results presented here, 60 elements were employed in the circumferential direction and one element in the thickness direction. Calculations performed with two elements in the thickness direction (120 total elements) showed no difference in the results with those with one element in the thickness direction. In performing the calculations for this set of parameters, it was found that the coupled calculation exhibits oscillations that were removed through the use of

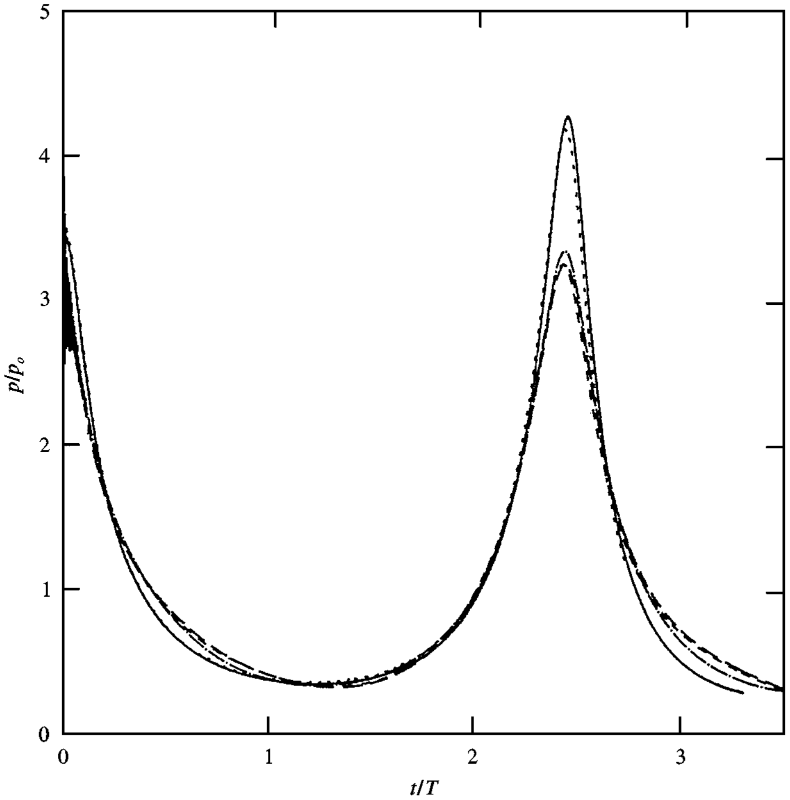

Figure 13. Bubble growth and collapse at a standoff of 1·5 $R_{\max}$ above a spherical structure: calculated pressures generated on structure node nearest the bubble for fixed, rigidly moving and deforming structure: ——, fixed; - - -, rigidly moving; — — — $\alpha_s = 10^{-3}$, $\alpha_m = 0$; ——— $\alpha_s = 10^{-4}$, $\alpha_m = 0$; —·—·—· $\alpha_s = 10^{-4}$, $\alpha_m = 140$.

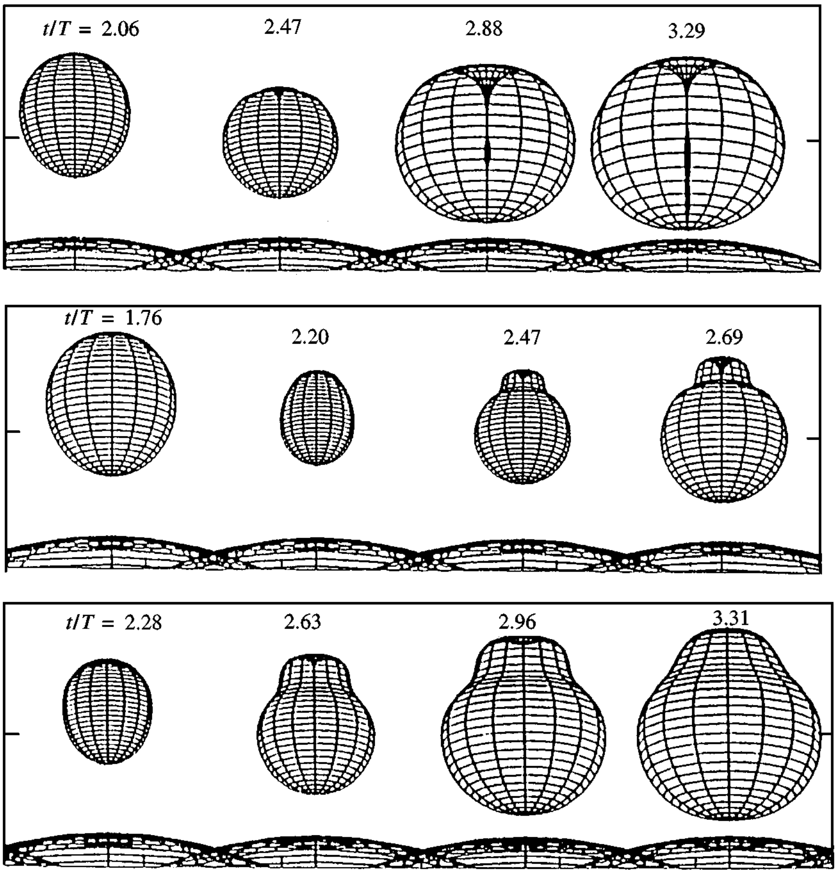

Figure 14. Comparison of calculated bubble shapes during collapse and rebound for three types of structural response for the case of Figure 13. Top: rigid fixed structure. Middle: rigid moving structure. Bottom: deforming moving structure.

Rayleigh damping for the structure as described in Kalumuck *et al.* (1995) and Chahine *et al.* (1997). Rayleigh damping can be expressed as

$$\xi_r = 0{\cdot}5\left(\frac{\alpha_m}{2\pi f_r} + \alpha_s 2\pi f_r\right). \tag{18}$$

Here, ξ_r is the fraction of critical damping of mode r of frequency f_r, and α_m and α_s are the mass and stiffness damping coefficients (given in units of s^{-1} and s, respectively). The former produces damping that varies inversely with frequency, while the stiffness damping varies directly with frequency.

The effects of structural motion and flexibility are presented in Figures 13–15. Calculated pressure histories at the structure node nearest the bubble are presented in Figure 13 for three structural conditions: fixed (rigid immovable), rigidly moveable and flexible. Calculations for three flexible structural damping conditions show little variation. The rigidly moving structure is seen to result in a slight reduction in the pressure generated, while

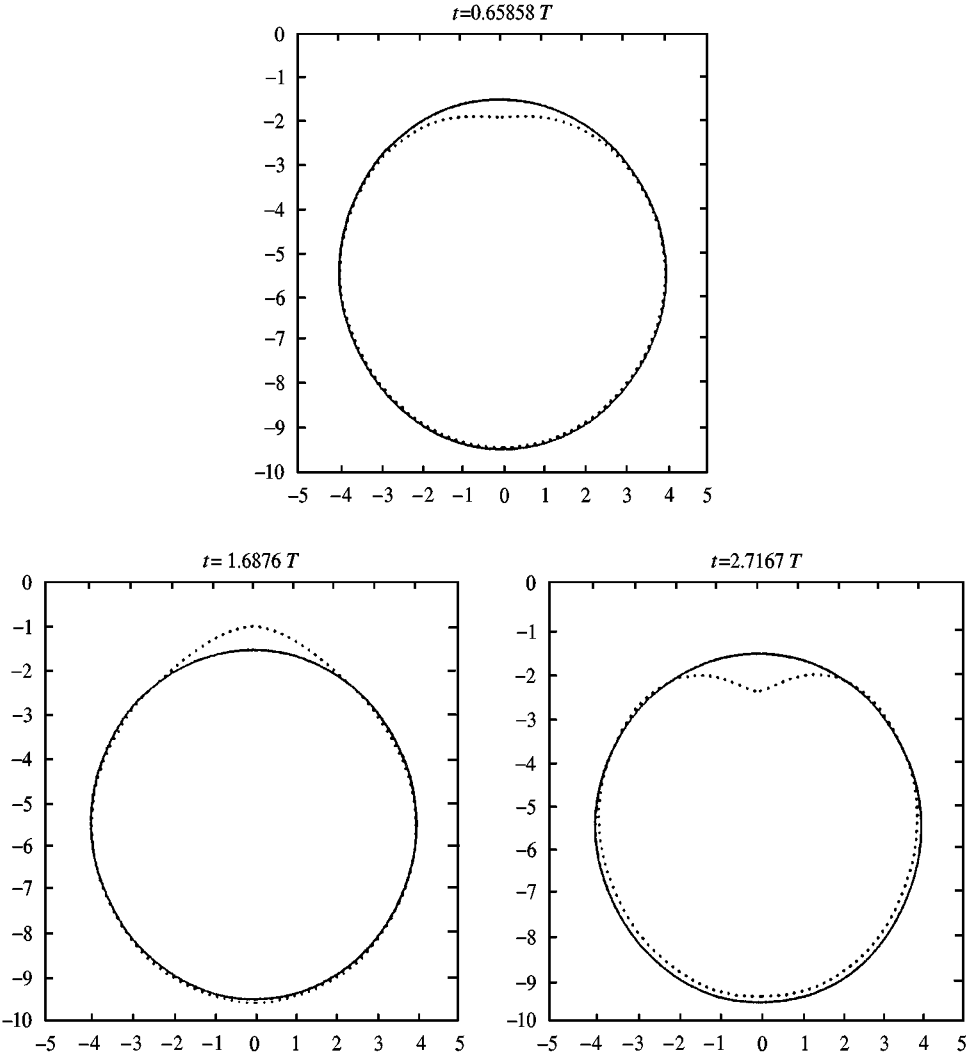
t=0.65858 T

t= 1.6876 T

t=2.7167 T

Figure 15. Deformed structure shapes at selected times for the case of Figures 13 and 14: . . . . , deformed shape, deformations exaggerated 25 times; ——, undeformed shape.

structural flexibility is seen to result in a *reduction of the peak pressure by about 25%* relative to the fixed or rigidly moving structure cases. The bubble period is shortened by both rigid-body motion and by structural flexibility as compared to the fixed case.

Figure 14 presents the bubble shapes at different times which exhibit a dramatic difference at the end of a bubble cycle of oscillation. In the rigid fixed body case the bubble collapses without significant jet formation, then forms a very thin jet during rebound. Best & Kucera (1992) found similar results near solid walls. Lauterborn (1981) has observed jet formation during rebound using laser-generated bubbles. Subsequent bubble growth is such that the bubble practically touches the structure by the time the very thin jet impacts it. For the rigidly moving structure, a constriction develops on the top of the bubble prior to development of the re-entrant jet. The later collapse of this constriction may correspond to the "counter-jet" observed in the experiments of Lauterborn & Bolle (1975). In the flexible wall case, a constriction also develops on the top of the bubble followed by the beginning of a re-entrant jet. However, the jet disappears as the bubble continues to grow during rebound.

The influence of the bubble on the structure can be seen in Figure 15 which presents the deformed structure shapes at three instants: during the growth, near maximum bubble size and near the end of the collapse. In this figure, *the deformations have been exaggerated by a factor of 25 for clarity*. The influence of the loading by the bubble is apparent. During the early growth and at the time of collapse, the portion of the structure nearest the bubble (top) is pushed away from the bubble. Between these times, this portion of the structure is drawn towards the bubble.

5. CONCLUSIONS

By the use of water slugs generated by well-characterized water jets under controlled conditions, the influence of structural flexibility on the loads generated by an impacting water jet on a solid wall have been assessed. Results of experiments conducted by impacting water jets of the same characteristics on "rigid" and "flexible" plates show a consistent decrease in the peak pressure load generated on the flexible plate relative to that of the rigid. At the highest jet pressure tested, plate flexibility produced a 40% decrease in the load generated relative to the rigid-plate case. Experiments were conducted over a range of operating conditions that provide consistent repeatable results. Results of simulations of bubble interaction with a nearby structure utilizing a coupled BEM hydrodynamics and FEM structural dynamics code similarly show a substantial reduction in loading on a flexible structure compared with a rigid structure as well as modification to the bubble dynamics.

These results highlight the need to utilize fully coupled calculations of explosion bubble loading on structures and the potential for error that can be present when applying a rigid-wall loading to a flexible structure to calculate its response.

ACKNOWLEDGEMENTS

This work was funded in part by the Naval Surface Warfare Center, Dahlgren Division, White Oak Detachment, under Contract No. N60921-92-C-0061.

References

Best, J. P. & Kucera, A. 1992 A numerical investigation of non-spherical rebounding bubbles. *Journal of Fluid Mechanics* **245,** 137–154.

Bourne, N. K. Obara, T. & Field, J. E. 1996 The impact and penetration of a water surface by a liquid jet. *Proceedings of the Royal Society of London* A **452,** 1497–1502.

Bourne, N. K., Obara, T. & Field, J. E. 1997 High speed photography and stress gauge studies of jet impact upon surfaces. *Philosophical Transactions of the Royal Society of London A* **355,** 607–623.

Chahine, G. L. & Duraiswami, R. 1993 Boundary element method for calculating 2-D and 3-D underwater explosion bubble behavior in free water and near structures NSWC Weapons Research and Technology Department Report NSWCDD/TR-93/44.

Chahine, G. L., Duraiswami, R. & Kalumuck, K. 1997 Boundary element method for calculating 2-D and 3-D underwater explosion bubble loading on nearby structures including fluid–structure interaction effects. NSWC Weapons Research and Technology Department Report NSWCDD/TR-93/46.

Chahine, G. L., Lambrecht, C., Kalumuck, K., Frederick, G. & Aley, P. 1995 An experimental study of the influence of structural deformation on water jet impact loading. Dynaflow, Inc. Technical Report 92001-7.

Den Hartog, J. P. 1952 *Advanced Strength of Materials*. New York: McGraw-Hill.

Engleman, B. & Hallquist, J. O. 1991 NIKE2D: a nonlinear, implicit, two-dimensional finite element code for solid mechanics, user's manual. Lawrence Livermore National Lab Report UCRL-MA-105413, Livermore, CA, U.S.A.

Harris, C. M. & Crede, C. E. 1976 *Shock and Vibration Handbook*, 2nd edition., New York: McGraw-Hill.

Kalumuck, K., Duraiswami, R. & Chahine, G. 1995 Bubble dynamics fluid-structure interaction simulation by coupling fluid BEM and structural FEM codes. *Journal of Fluids and Structures* **9,** 861–883.

Kiddy, K. C. & McDonald, W. W. 1994 Response of deformable cylinder models to underwater explosion bubble collapse loading. Summary of $\frac{1}{35}$-Scale Structural Response Calculations (U). NSWCDD/TR-93/24 (Confidential).

Lauterborn, W. 1981 Cavitation bubble dynamics—new tools for an intricate problem. In *Mechanics and Physics of Bubbles in Liquids*, IUTAM Symposium Proceedings (ed. L. Van Wijngaarden), pp. 165–178.

Lauterborn, W. & Bolle, H. 1975 Experimental investigations of cavitation bubble collapse in the neighborhood of a solid boundary. *Journal of Fluid Mechanics* **72,** 391–399.

Lesser, M. B. 1981 Analytical solutions of liquid-drop impact problems. *Proceedings of the Royal Society of London A* **377,** 289–308.

Oguz, H. N., Prosperetti, A. & Kolaini, A. R. 1995 Air entrapment by a falling water mass. *Journal of Fluid Mechanics* **294,** 181–207.

Timoshenko, S. & Woinowsky-Krieger, S. 1959 *Theory of Plates and Shells*. New York: McGraw-Hill.